

Highlighting the effect of the aluminium alloy self-corrosion on the AA2024-T3/Ti6Al4V galvanic coupling in NaCl media

L.B. Coelho^{a,*}, M. Hacha^a, Y. Paint^b, M.-G. Olivier^{a,b}

^a Materials Science Department, Faculty of Engineering, University of Mons, 20 Place du Parc, 7000 Mons, Belgium

^b Materia Nova asbl, Avenue Copernic 1, 7000 Mons, Belgium

ARTICLE INFO

Keywords:

Alloys
Galvanic corrosion
AA2024
Ti6Al4V
SVET
ZRA

ABSTRACT

The corrosion mechanism of an AA2024-T3/Ti6Al4V galvanic couple model (electrodes' area ratio = 1) was investigated in NaCl media by means of Scanning Vibrating Electrode Technique (SVET), Zero Resistance Ammeter (ZRA), potentiodynamic polarisation and Open Circuit Potential (OCP) analysis. Galvanic coupling was not sufficiently intense to impact the self-corrosion process of AA2024 exposed to 0.01 M or 1 M NaCl solution. Scanning Electron Microscopy and Energy Dispersive X-ray Spectroscopy (SEM-EDX) clearly demonstrated that trenching of the AA2024 matrix induced by its constituent inclusions was the main corrosion process concerning the couple. The highly stable passive layer of Ti6Al4V, which was shown to present a poor catalytic nature for oxygen reduction, was responsible for the limited extension of galvanic corrosion observed.

1. Introduction

By virtue of their attractive mechanical properties, materials such as Carbon Fibre Reinforced Polymers (CFRPs) and aluminium and titanium alloys have received particular attention in the creation of light-weight designs [1,2]. Titanium alloys possess outstanding properties, namely strength-to-weight ratio, super-plasticity, excellent corrosion resistance, which have led them to be used as structural materials in biomedical, marine, auto, chemical, aviation and aerospace industries [3–5].

A current strategy of the aeronautics industry for reducing fuel consumption is the combination of these light materials, creating hybrid structures. For instance, aluminium alloys are widely used for the production of aircraft wings and fuselages, while titanium alloys are preferred for critical fasteners and rivets often joining Al alloys to CFRP materials [6]. Such multi-material combinations require appropriate joining technologies in order to avoid galvanic corrosion induced by the electrochemical dissimilarities of the components [1,6]. Although a direct contact between Al alloys and composites is often prevented by insulating sheets, they can still be electrically connected if fasteners are conductive (e.g., Ti6Al4V bolt) [7,8].

An extensive amount of studies has focused on the galvanic corrosion behaviour of CFRP coupled either with Al alloys or with Ti alloys. With respect to the first case, coupling with carbon fibres were shown to considerably accelerate the corrosion intensity of different Al alloys

[1,2,9–14]. Regarding the Ti6Al4V/CFRP galvanic pair, it was demonstrated by several works that Ti6Al4V can be safely coupled to carbon fibre-based composites when exposed to NaCl media [12,15–18].

Despite the great interest of employing AA2024 for light-weight structural applications, this high-strength aluminium alloy has a main disadvantage: its sensitivity to pitting corrosion in chloride-containing media, which directly impacts its structural integrity [1]. On the other hand, titanium and its alloys present an extraordinary resistance to corrosion in saline and strongly oxidizing media [3]. Their high resistance is attributed to the formation of a compact, chemically stable and tightly adherent passive layer (mainly composed of TiO₂), which is spontaneously formed in the presence of oxygen [3–5]. In addition, in case of disruption of the passive film, it is almost instantaneously healed if traces of moisture or oxygen are present (it is only attacked by hot and concentrated reducing acids [19]).

Among titanium alloys, Ti6Al4V is the one most frequently used for engineering applications, representing more than half of the overall worldwide Ti usage [4,20]. It is most widely employed as a duplex structured alloy, which contains a hexagonal close-packed α phase (stabilized by Al) and a body-centred cubic β phase (stabilized by V). Different microstructures can be achieved depending on the heat treatment and 1350 MPa of ultimate strength can be reached [4,20,21]. The passive film formed on the Ti6Al4V alloy predominantly comprises TiO₂ enriched by alloying elements oxides, such as vanadium/

* Corresponding author.

E-mail address: leonardo.bertoluccicoelho@umons.ac.be (L.B. Coelho).

aluminium oxides [20].

Surprisingly, very little work has been devoted to the corrosion aspects related to the galvanic coupling between Al alloys and Ti alloys [22]. As a significant potential difference exists between both alloys in 3.5% NaCl (~ 0.38 V [23]), galvanic corrosion can occur if an electrical path is provided through a junction exposed to aggressive electrolytes [6]. In this work, aiming at simulating the galvanic coupling behaviour of an Al alloy plate/Ti alloy fastener bolt – such as currently encountered in aeronautics - an AA2024/Ti6Al4V couple model was evaluated in NaCl solution by means of SVET, ZRA, potentiodynamic polarisation and OCP analysis.

2. Materials and methods

2.1. AA2024/Ti6Al4V galvanic couple model

A galvanic couple model comprising AA2024 and Ti6Al4V was elaborated to simulate a multi-material junction often encountered in aircrafts fuselage. The nominal composition (in weight) of the Q-Lab AA2024-T3 plate was: 4.6% Cu, 1.9% Mg, 0.61% Mn, 0.19% Fe, 0.13% Zn (Si, Cr and Ti $< 0.02\%$) and balance Al. The 1 mm thick Al alloy plate was cut so as to obtain a coupon with a cross-section of $\sim 7 \times 1$ mm² (the specimen was subsequently cleaned in acetone/ethanol ultrasonic bath). The Ti6Al4V ELI alloy (UNS R56401, ASTM grade 23) was purchased from Ti-shop. The nominal composition (in weight) of the 3.0 mm diameter rod was: 6.2% Al, 4.1% V, 0.22% Fe, minor amounts of O, N, H and Ti balance. The AA2024 coupon was mounted in parallel to the Ti6Al4V rod using epoxy resin and a ~ 0.5 mm gap was left between them. The final area ratio between both specimens was equal to 1 (Fig. 1(a)). The attacked microstructures of AA2024 and Ti6Al4V were analysed by optical microscopy (Hirox 3D Digital Microscope), as shown in Fig. 1(b) and (c), respectively. Cu-rich intermetallic inclusions could be observed in the Al alloy, as indicated by an arrow. Concerning Ti6Al4V, a very fine discontinuous β phase was detected along with a continuous α phase.

The electrical connection between the mounted and separated alloy specimens was made by connecting individual Cu wires to their back sides. The loose ends of the Cu wires were connected either to each other (SVET tests) or to a potentiostat (ZRA analysis). Prior to testing, the model surface was ground using SiC paper (up to the 2000 grade) followed by ethanol/distilled water rinsing and compressed air drying.

2.2. SVET measurements

SVET was employed to investigate the galvanic coupling behaviour of the AA2024/Ti6Al4V model in aerated 0.01 M NaCl solution (pH ≈ 5.6 , conductivity $k \approx 1200$ $\mu\text{S cm}^{-1}$, volume ≈ 800 mL). The commercial equipment used was supplied by Uniscan (model SCV370). A Pt probe with a ~ 50 μm diameter tip vibrated in the vertical plane (Z) at a frequency of 80 Hz. The probe was positioned ~ 180 μm above

the sample surface and its vibration amplitude was 30 μm (peak-to-peak). The scan speed was 500 $\mu\text{m/s}$, the step size was 100 μm and the sensitivity was 800 μV . The scanned area was equal to 9×11 mm², which resulted in a ~ 30 min run. One first scan was performed immediately after immersion and was followed by 23 runs (1 run per hour, 30 min of waiting time between runs), resulting in a total immersion time of 24 h. This testing procedure was repeated twice and achieved results were reproducible. The connection between both alloy specimens was systematically checked prior to SVET testing using a multimeter.

2.3. ZRA measurements

Zero Resistance Ammeter (ZRA) tests were carried out with the AA2024/Ti6Al4V model to monitor the galvanic current and the galvanic potential (OCP of the couple) in aerated 0.01 M NaCl or 1 M NaCl electrolytes. An AMETEK Parstat 2273 supported by Powersuite® software was employed. Working in ZRA mode, the AA2024 specimen was connected as the working electrode (WE) while the Ti6Al4V specimen was connected to the earth, inside a Faraday Cage. An Ag/AgCl/KCl_{sat} (+197 mV/SHE) was employed as reference electrode (the RE was positioned ~ 0.5 cm from the sample surface). For this given configuration, a positive current measured means that a net negative charge leaves the Al alloy and flows through the potentiostat towards the Ti alloy. In this case, as the alloys area ratio was equal to 1, the galvanic currents were divided by the area of the electrodes to be expressed in current density ($\mu\text{A/cm}^2$). ZRA measurements lasted 90 min and were performed in duplicate.

2.4. OCP and potentiodynamic polarisation testing

OCP analysis and potentiodynamic polarisation tests were performed separately for AA2024 and Ti6Al4V in aerated 0.01 M NaCl medium. One Al alloy and one Ti alloy specimens (areas = ~ 0.07 cm²) similar to those employed for the model were separately mounted in two moulds using epoxy resin (their surfaces were prepared according to the same procedure used for the model). By employing the AMETEK Parstat 2273, polarisation curves were acquired at a scan rate of 0.83 mVs⁻¹, after an OCP analysis period of 60 min. The electrochemical cell (placed in a Faraday cage) comprised either AA2024 or Ti6Al4V as WE, an Ag/AgCl/KCl_{sat} (+197 mV/SHE) as RE and a Pt coil as counter electrode. Both anodic and cathodic polarisation branches were executed separately starting from OCP for the Al alloy, while only the cathodic branch was obtained for the Ti alloy. Measurements were performed at least in duplicate.

2.5. SEM–EDX analysis

Scanning Electron Microscopy (SEM) investigations were carried out using a Hitachi SU8020 microscope coupled to an Energy Dispersive

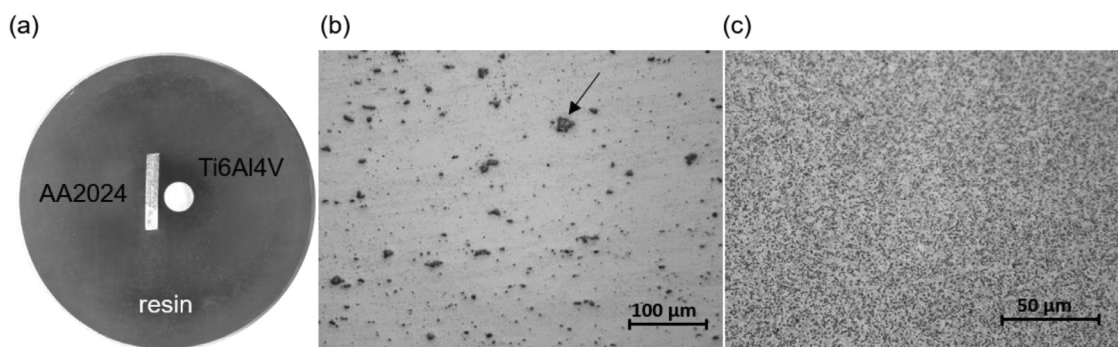


Fig. 1. (a) Ground surface of the AA2024/Ti6Al4V galvanic couple model (area ratio = 1). Optical micrographs (Hirox 3D Digital Microscope) from the reference ground surfaces of AA2024 (b) and Ti6Al4V (c).

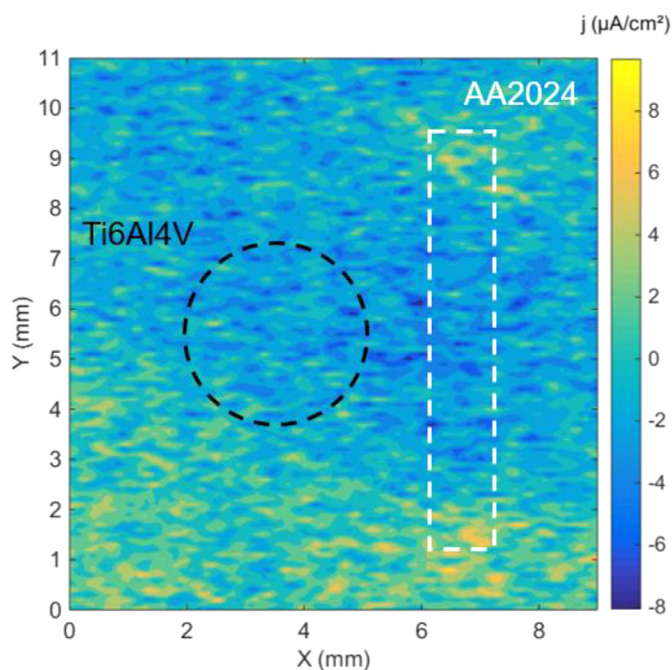


Fig. 2. SVET current density ($j / \mu\text{A cm}^{-2}$) map obtained from the AA2024/Ti6Al4V galvanic couple after 20 h of immersion in 0.01 M NaCl electrolyte.

X-ray Spectrometer analyser (EDX). Surface analyses were performed on the AA2024/Ti6Al4V model prior (freshly ground surface state) and after SVET testing. The surface of the corroded sample was rinsed with distilled water prior to analysis.

3. Results and discussion

3.1. SVET testing supported by surface analysis

SVET was employed to depict the electrochemical activity distribution related to the surface of the AA2024/Ti6Al4V galvanic couple model. The current density map presented in Fig. 2 was obtained after 20 h of exposure to 0.01 M NaCl. The positions occupied by the AA2024 and Ti6Al4V specimens appeared identified by white and black dashed lines, respectively.

Galvanic corrosion related to the AA2024/Ti6Al4V model could not be clearly identified. Indeed, no localised activity could be attributed to the location occupied by the Ti alloy. Concerning the Al alloy, only weak spots of anodic activity located on the extremities of the coupon and a slight cathodic process on the remaining regions could be detected. Contrarily to the expected, these results suggest that Ti6Al4V was not a preferential site for cathodic reactions when electrically connected to AA2024. Or at least, it could be attested that if any galvanic process took place, its intensity was below the sensitivity of the technique (inferior to $\pm 1 \mu\text{A/cm}^2$). Different j maps obtained throughout 24 h of immersion were either similar to the one presented in Fig. 2 or presented even less intense activities.

Visual inspection during and after immersion showed clear traces of corrosion on AA2024, while the Ti6Al4V surface remained apparently unaltered. The reason for which SVET was not able to highlight the self-corrosion of AA2024 was reflective of the localised nature of this process, in which the distances between local cells are often too small to be sensed by the probe [24] - although the present analysis eventually depicted regions operating preferentially as anode or cathode, indicating that the Al alloy behaved as a mixed electrode. Concerning Ti6Al4V, the development of pitting (breakdown of the passive film) would only be expected to take place in NaCl medium by applying extremely elevated anodic overpotentials [3,25]. Although no corrosion

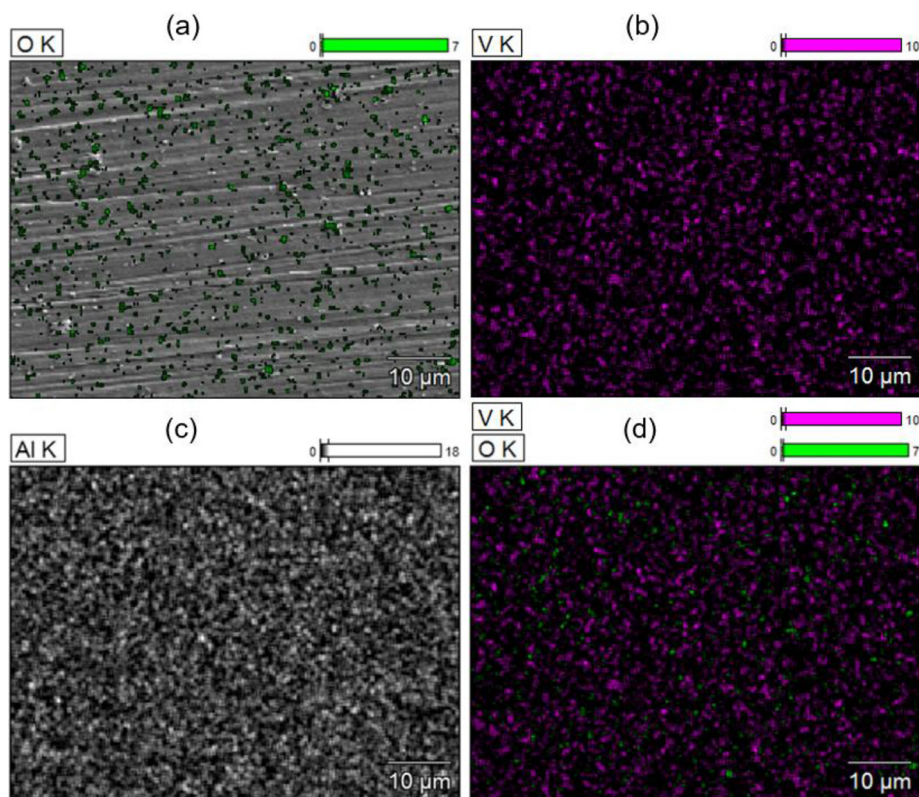


Fig. 3. SEM images and EDX elemental mapping of Ti6Al4V from the galvanic couple after 24 h of exposure to 0.01 M NaCl. (a) SEM-EDX composite image displaying the O distribution map. (b) V and (c) Al distribution maps. (d) Composite image of the O and V distribution maps.

signs were identified on Ti6Al4V after the test (24 h in 0.01 M NaCl), SEM–EDX mapping analysis showed the presence of oxygen on a few regions (Fig. 3(a)) (in comparison, no detectable amount of oxygen was found by applying the same approach on a reference Ti6Al4V surface). The enrichment of oxygen was most likely related to the formation/growth of oxide phases referred as responsible for further improving the passivation properties of the alloy [3–5]. Moreover, V presented a preferential distribution (Fig. 3(b)), while Al was rather homogeneously detected on the entire surface (Fig. 3(c)) (Al has a high solid solubility in both α and β phases [20]).

Fig. 3(d) shows that oxygen was mainly detected at interfacial regions between the α and β phases, presenting particularly high signals on the α phase. According to the work of Textor on the passive layer properties of Ti6Al4V [26], the Al_2O_3 phase mainly placed on the surface of the α domain might be unstable in the presence of chloride ions. Similarly, Yang et al. reported that the β phase presents a higher corrosion resistance in comparison to the α phase [25]. Finally, the difference in V composition of the α and β phases suggests possible local galvanic interactions, resulting in the increased reactivity of α/β phase boundaries [3]. Thus, the preferential location of oxygen at α/β phase boundaries is likely reflective of the superior kinetics of Al_2O_3 formation at these interfaces. Similarly, Fig. 4 shows SEM images and corresponding EDX elemental maps obtained on AA2024 from the model after the 24 h SVET test performed in 0.01 M NaCl.

Contrary to the Ti6Al4V case, corrosion product domes were clearly observed on the surface of the Al alloy (Fig. 4(a)). Besides Al, these precipitates were mainly constituted of O and Cl (Fig. 4(b) and (c), respectively), likely referring to Al (hydr)oxide/hydroxychloride phases [9]. The remarkable volume occupied by the dome was translated by the shadowed region (absence of signal) right next to it. Moreover, trenching of the alloy matrix around intermetallic particle (IMPs) was undoubtedly assigned (Fig. 4 (a) and (d)). Cu-rich remnants were left on the centre of the formed grooves, as indicated by the EDX elemental map of Cu (Fig. 4(e)). Based on the round shape of this particular Cu-rich remnant, it probably originated from an Al_2CuMg particle [9,27]. The backscattered electron image in Fig. 4(f) shows remnant particles in more detail: trenches were formed on the matrix through an axial

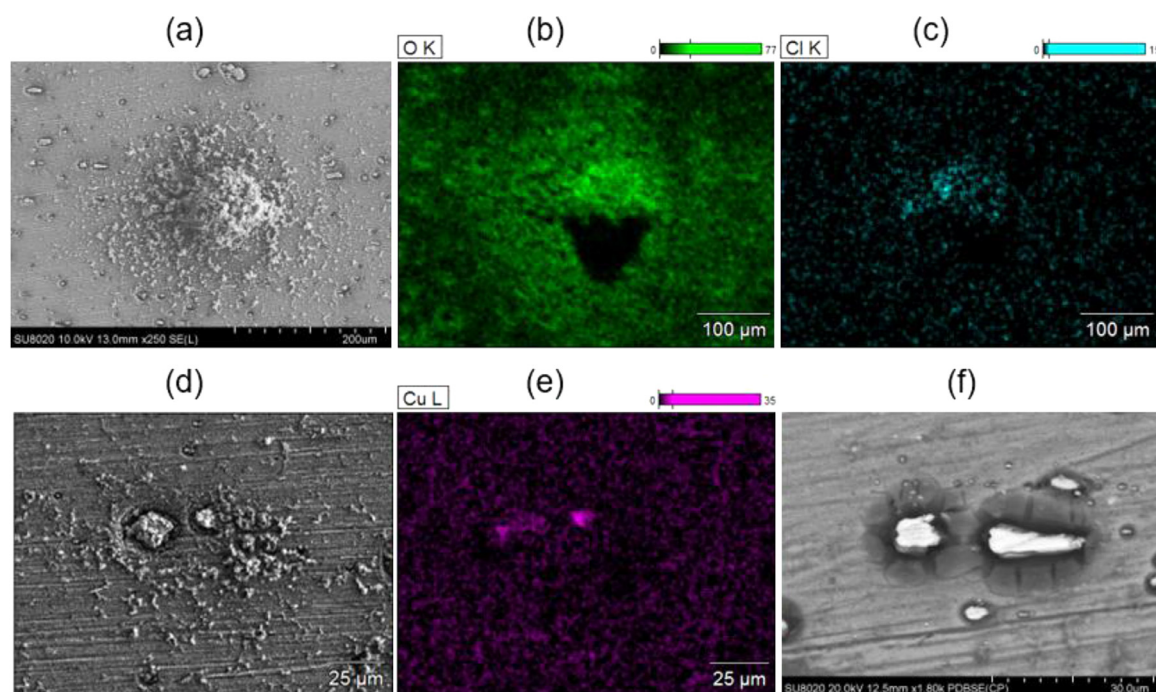


Fig. 4. SEM images and EDX elemental mapping of AA2024 from the galvanic couple after 24 h of exposure to 0.01 M NaCl. (a, b, c) secondary electron image and corresponding distributions maps of O and Cl. (d, e) secondary electron image and corresponding distribution map of Cu. (f) Backscattered electron image.

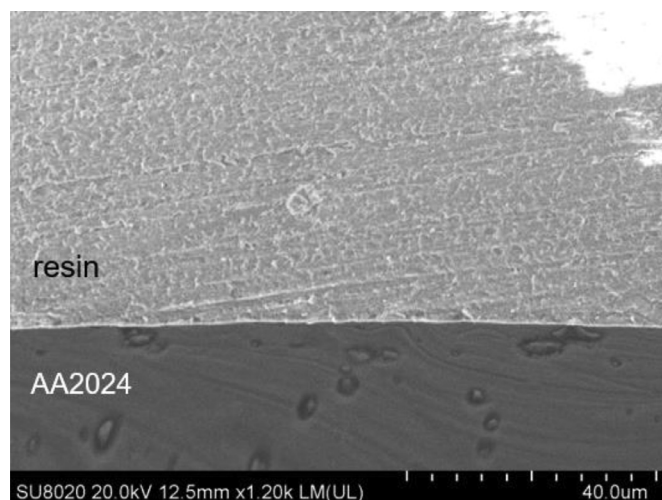


Fig. 5. SEM image from the AA2024/resin interface region of the galvanic couple model after 24 h of exposure to 0.01 M NaCl.

growth from the particles. The darker zones identified around them were reflective of a process of local impoverishment in Cu, which renders the matrix locally more susceptible to anodic attack. Thereby, the adjacent matrices corroded because of coupling with Cu-rich IMPs that catalysed the reduction of oxygen. Concerning the S-phase, it is known to trigger Cu redeposition processes that also induce the local attack of the matrix nearby Cu-rich remnants [28,29]. In all cases, the morphology of corrosion observed for AA2024 was typical of localised corrosion induced by Cl^- and driven by micro-galvanic interactions.

SEM analysis was also performed at the AA2024/resin interface, in the resin region separating both alloys. No corrosion products were detected at this frontier region, as demonstrated in Fig. 5. This fact is a strong indication that no significant galvanic coupling was established between AA2024 and Ti6Al4V. On the contrary, corrosion products should most likely have precipitated over the resin surface separating both specimens, as it often the case for galvanic coupling models

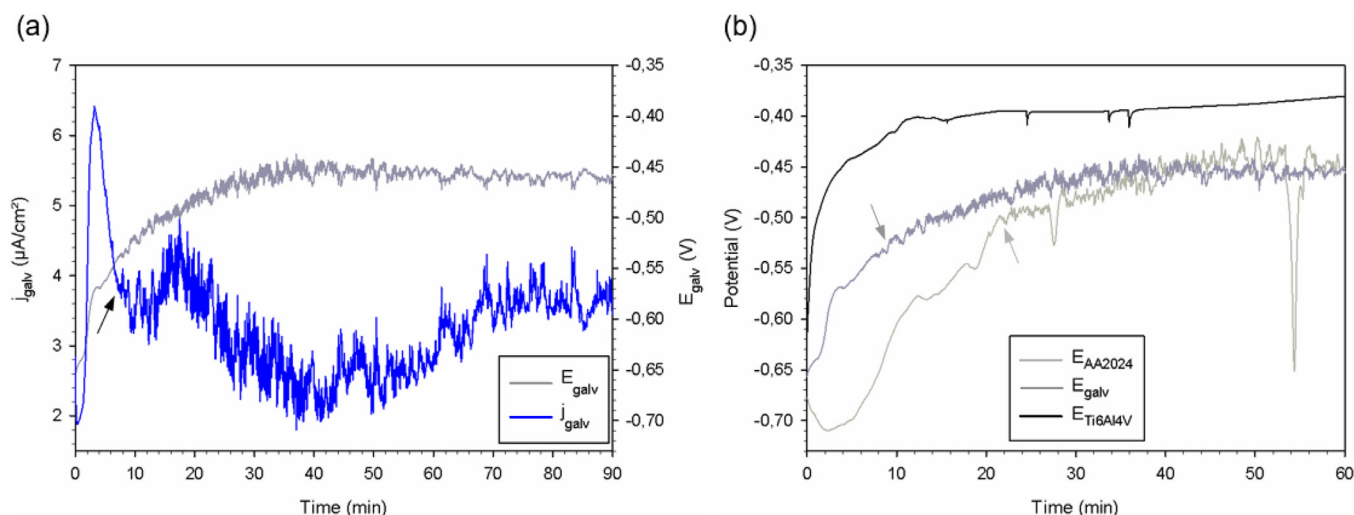


Fig. 6. (a) j_{galv} ($\mu\text{A}/\text{cm}^2$) and E_{galv} (V vs Ag/AgCl/KCl_{sat}) curves obtained by ZRA for the AA2024/Ti6Al4V galvanic couple immersed in 0.01 M NaCl. (b) Comparison of E_{galv} with the OCP curves of AA2024 and Ti6Al4V obtained in 0.01 M NaCl solution.

comprising separated components [9,10,30]. Therefore, in the present case, it could be said that the connection of these dissimilar alloys did not alter the corrosion mechanism of an alloy mainly subjected to a self-corrosion process.

3.2. ZRA and OCP analyses

Seeking at understanding the reason for the absence of a clear galvanic process between the Al and Ti alloys, conventional electrochemical techniques (not localised ones) were carried out employing a potentiostat. First, ZRA measurements were performed to determine the galvanic current density j_{galv} and the galvanic potential E_{galv} (OCP) of the couple, as a function of time.

Fig. 6(a) shows the evolution of both j_{galv} and E_{galv} during 90 min of exposure to 0.01 M NaCl. As AA2024 was chosen to be the working electrode, the positive values of j_{galv} obtained mean that the overall activity on this alloy was preferentially anodic. Thus, the surplus of anodic reactions should be matched by corresponding cathodic reactions occurring on the Ti6Al4V surface. However, one should realise the relative insignificance of the j_{galv} values obtained, namely, $\sim 2 \mu\text{A}/\text{cm}^2$ after 40 min. In other words, the anodic dissolution of the alloy specifically induced by coupling with the Ti alloy could be considered as irrelevant - except for the first 10 min of test. For instance, in the beginning of immersion, j_{galv} had risen to $6.4 \mu\text{A}/\text{cm}^2$ before a rapid decrease to $\sim 3.6 \mu\text{A}/\text{cm}^2$. It was interesting to note that the j_{galv} peak occurred simultaneously to a progressive increase in E_{galv} . Indeed, the corrosion potential started at ~ -0.65 V and increased up to ~ -0.55 V after 10 min. From this time on, the E_{galv} demonstrated great fluctuation, which lasted for the entire duration of the test, even when relatively steady potentials (~ -0.45 V) were reached after 30 min. This continuous increase in potential might be related to the precipitation of corrosion products on AA2024, such as highlighted in the SEM images (Fig. 4). Similar potential evolutions obtained for AA2024 in NaCl solutions [31,32] were attributed to the formation of a porous oxide layer triggered by chloride ions attack.

The current transients simultaneously observed in the j_{galv} curve are attributed to localised corrosion events, such as metastable and stable pitting events [27,33]. The creation of local active areas (pits) through the passive layer of AA2024 explains the oscillations in the OCP response. The dealloying process of the Al₂CuMg is also referred as responsible for potential oscillations [27,34], being the onset of pitting often associated to the locations of these inclusions [35]. Therefore, it is suggested that the self-corrosion of AA2024 occurs with significant

intensity only after ~ 10 min of immersion, following the initial j_{galv} peak, as indicated by an arrow in Fig 6(a). This activation period seems to be reflective of the time needed for the passive layer to be completely disrupted, resulting in a generalised exposition of the underlying metallic substrate.

Fig. 6(b) compares the potential evolution of the couple (E_{galv}) with the OCPs of Ti6Al4V and AA2024 (E_{AA2024} and E_{Ti6Al4V} , respectively) obtained in 0.01 M NaCl solution. It could be seen that the E_{galv} curve was quite like the E_{AA2024} curve, apart from the fact that the curve of the model was shifted to the left (towards earlier times). Indeed, while the activation period for the couple was around 10 min, the corresponding period for AA2024 was around 20 min (both periods are indicated by an arrow in Fig. 6(b)). Therefore, it seemed that the breakdown of passivity occurred faster on the Al alloy in case of coupling with Ti6Al4V. Nonetheless, once pitting started to take place on AA2024, E_{galv} and E_{AA2024} became nearly coincident, meaning that the Al alloy from the model also started to corrode under OCP conditions. As the OCP and the pitting potential of AA2024 can be considered as coincident in NaCl medium, only a minor anodic overpotential would be necessary to promote pitting propagation. After all, the self-corrosion of AA2024 triggered by Cu-rich inclusions appeared to be the governing factor regardless the connection with Ti6Al4V.

With respect to the potential evolution of Ti6Al4V solely, it remained stable at ~ -0.4 V already after 15 min. The E_{Ti6Al4V} curve was much less noisy than the curves of the AA2024-containing samples, which suggested the less active electrochemical behaviour of the Ti alloy under the present conditions. Very low corrosion currents were expected for Ti6Al4V under OCP conditions, because TiO₂ presents a high ohmic resistivity combined to an outstanding resistance to chlorides [18,20]. Even in the case of Ti6Al4V from the model, spontaneous passivity was rather expected, as the OCP values achieved were well within the range of TiO₂ thermodynamic stability [3,20]. The positive shift of E_{Ti6Al4V} observed in the first 15 min of exposure was indicative of improved passivity resulting from the formation/growth of oxide phases mainly based on TiO₂ as well as Al₂O₃/V-oxides [3–5,20].

After 1 h of immersion, the potential difference between the Ti alloy and the Al alloy was around 0.05 V. In general, it can be considered that if the potential difference between two materials is less than 0.05 V, the galvanic corrosion can be neglected [36]. Nevertheless, as Ti6Al4V was able to induce a faster disruption of the passive layer of AA2024, it means that both alloys were subjected to a galvanic coupling process – despite its minor intensity. Particularly in the beginning of immersion, cathodic reactions on the Ti alloy might have supported an anodic

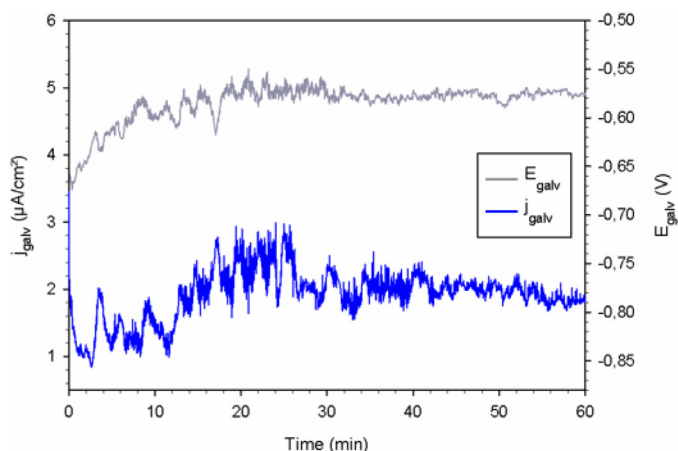


Fig. 7. j_{galv} ($\mu\text{A}/\text{cm}^2$) and E_{galv} (V vs Ag/AgCl/KCl_{sat}) curves obtained by ZRA for the AA2024/Ti6Al4V galvanic couple immersed in 1 M NaCl solution.

overpotential on the Al alloy. According to different authors [33,37], the higher the anodic potential applied to AA2024, the higher the rate of pitting nucleation.

As the galvanic coupling effect observed for the AA2024/Ti6Al4V model was rather limited in 0.01 M NaCl electrolyte, ZRA tests were repeated in 1 M NaCl media. This solution was chosen not only to increase the concentration of aggressive species but also to improve its conductivity, reducing possible ohmic drop effects.

The curves obtained from the ZRA monitoring in 1 M NaCl (Fig. 7) show the evolution of j_{galv} and E_{galv} . The positive currents achieved once again testified that AA2024 behaves preferentially as an anode when coupled to Ti6Al4V. The j values achieved in this case were as low as those obtained in 0.01 M NaCl (around $+2 \mu\text{A}/\text{cm}^2$). Regarding the potential evolution, it presented quite the same trend as observed in the less aggressive electrolyte; although here E_{galv} values measured were significantly lower, reaching values around -0.58 V after 20 min. As expected, the increase in chloride concentration lowers the corrosion potential of AA2024 [2] which might have contributed for the lower E_{galv} in this case.

The main difference in the present case was that current transients (and potential oscillations) appeared immediately upon immersion. This finding suggested that, due to the higher NaCl concentration, pitting of the Al alloy occurred starting from the beginning. Hence, also in 1 M NaCl solution, the low j_{galv} values obtained might once more be explained by the self-corrosion of AA2024: the electrons generated from the anodic dissolution of Al, instead of flowing through the external circuit of the potentiostat (and reach Ti6Al4V), would be directly consumed by ORR occurring on the Cu-rich intermetallics. In all cases, the increase in the NaCl concentration did not seem to affect the intensity of the galvanic corrosion process of the model.

3.3. Potentiodynamic polarisation curves

In order to simulate the influence of the anodic and cathodic processes related to AA2024 and Ti6Al4V in case of galvanic couple formation, potentiodynamic polarisation tests were carried out separately on the two alloys. More particularly, anodic and cathodic polarisation curves were achieved for AA2024, while only the cathodic branch was obtained for Ti6Al4V (Fig. 8).

First, as these polarisation curves started from the correspondent alloys' OCP, they allowed the confirmation of the potential values achieved after 1 h (Fig. 6): $\sim -0.40 \text{ V}$ and $\sim -0.45 \text{ V}$ for Ti6Al4V and AA2024, respectively. Concerning the E_{galv} and j_{galv} , these could be estimated by the intersection between the cathodic curve of Ti6Al4V and the anodic curve of AA2024. Once again, the estimated E_{galv} did not considerably differ from E_{AA2024} . By extrapolation of the anodic curve,

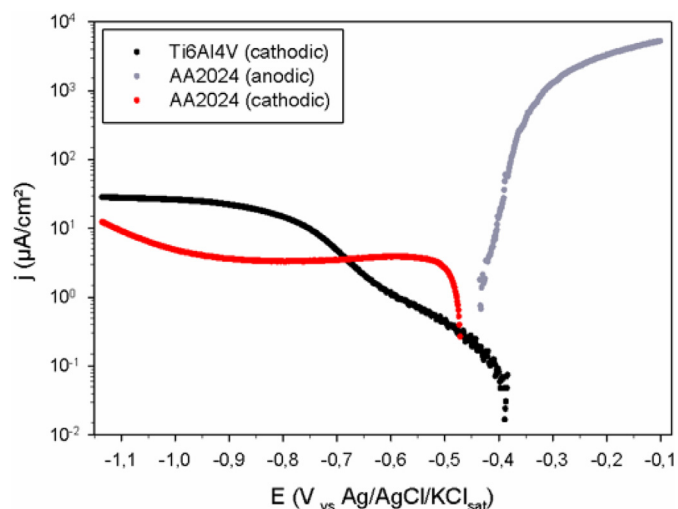


Fig. 8. Potentiodynamic polarisation curves obtained from Ti6Al4V (cathodic) and from AA2024-T3 (anodic and cathodic) in 0.01 M NaCl solution.

the j_{galv} seemed to be around $1 \mu\text{A}/\text{cm}^2$, which is in accordance with the ZRA results.

Most importantly, it could be seen that for potential values close to the estimated E_{galv} , the kinetics of oxygen reduction reaction (ORR) was much higher on AA2024 than on Ti6Al4V. For instance, at $\sim -0.45 \text{ V}$, the cathodic current densities achieved were about one order of magnitude higher on the Al alloy than on the Ti alloy. As pointed out by Atapour et al. [3], the poor catalytic nature of the Ti oxide surface is responsible for the resulting low kinetics of ORR, which also explains the corrosion resistance of Ti alloys. Only at much lower potentials (below $\sim -0.70 \text{ V}$), the cathodic response from Ti6Al4V exceeded that from AA2024, due to the rise of a favoured kinetics of water reduction reaction [3]. Similar outcomes were obtained by Mansfeld et al. [22] by superimposing the anodic and cathodic curves for AA2024 with the cathodic curve for Ti6Al4V: the estimated current density simulating an Al alloy/Ti alloy coupling was about 1 order of magnitude lower than the measured j_{corr} for AA2024.

The greater kinetics of ORR verified for AA2024 resulted of its constituent Cu-rich inclusions. Hence, these polarisation curves illustrate why AA2024 presented self-corrosion even when connected to Ti6Al4V: once the passive layer of the Al alloy is disrupted, the progressively exposed Cu-rich surfaces became the main support for ORR. Moreover, the absence of a passive region in the anodic curve of AA2024 (Fig. 8) highlighted its great susceptibility to pitting (OCP coincident to pitting potential) and consequent generation of Cu-rich remnants. As illustrated by Miller Jr. by plotting together the cathodic curves obtained for Cu and Ti in NaCl solution [18], Cu is a much more effective electrode for the reduction of oxygen than Ti. In the case of the considered model, it is also worthy of mention that the resin gap ($\sim 0.5 \text{ mm}$) between both alloys certainly complicated the ion transport kinetics between them, further favouring the more direct galvanic reactions between the AA2024 matrix and its inclusions.

4. Conclusions

This local investigation supported by conventional electrochemical techniques and surface analysis revealed important information on the corrosion behaviour of an AA2024/Ti6Al4V galvanic couple model. ZRA results demonstrated that the magnitude of galvanic corrosion between AA2024 and Ti6Al4V is not significant when the exposed areas of both alloys is similar, in both diluted (0.01 M) or concentrated (1 M) NaCl solution. The only substantial effect induced by galvanic coupling was the faster disruption of the AA2024 passive layer, as depicted in the first minutes of the OCP analysis carried out in 0.01 M NaCl.

Nonetheless, as indicated by SEM–EDX analysis performed after a 24 h SVET test, the Al alloy seemed to be subjected only to a self-corrosion process. Indeed, the resulting surface of AA2024 presented typical features of localised attack induced by micro-galvanic coupling formation between Cu-rich intermetallics and the matrix. Concerning Ti6Al4V, it did not show appreciable traces of corrosion, apart from a process of selective enrichment in oxygen located at α/β phase boundaries.

Furthermore, the effect of galvanic coupling was simulated by superimposing the anodic polarisation curve of AA2024 with the anodic/cathodic branches of Ti6Al4V. It was suggested that an effective galvanic coupling between both alloys did not take place because the kinetics of ORR is much higher on AA2024 than on the Ti alloy. Once pitting initiates on the Al alloy, the increasingly higher exposition of Cu-rich surfaces could efficiently drive the cathodic process from Ti6Al4V to AA2024. Hence, contrarily to thermodynamic predictions, galvanic corrosion of the AA2024/Ti6Al4V couple could be considered as negligible in NaCl media by virtue of the low kinetics of ORR on Ti oxide when compared to that on metallic Cu. Finally, as this work considered only one galvanic couple model (electrodes' area ratio = 1), it cannot be indistinctly anticipated that galvanic corrosion could not be problematic in case of more severe configurations, such as higher Ti6Al4V/AA2024 area ratios or both alloys in direct contact.

Acknowledgements

The author L.B. Coelho acknowledges the Research Institute of Materials Science and Engineering of University of Mons for financial support and Mr. Michel Princen from Sonaca Group for indicating the relevance of the covered topic.

Supplementary materials

Supplementary material associated with this article can be found, in the online version, at [doi:10.1016/j.surf.2019.04.004](https://doi.org/10.1016/j.surf.2019.04.004).

References

- Mandel, L. Krüger, Determination of pitting sensitivity of the aluminium alloy EN AW-6060-T6 in a carbon-fibre reinforced plastic/aluminium rivet joint by finite element simulation of the galvanic corrosion process, *Corros. Sci.* 73 (2013) 172–180, <https://doi.org/10.1016/j.corsci.2013.03.033>.
- S. Palani, T. Hack, J. Deconinck, H. Lohner, Validation of predictive model for galvanic corrosion under thin electrolyte layers: an application to aluminium 2024-CFRP material combination, *Corros. Sci.* 78 (2014) 89–100, <https://doi.org/10.1016/j.corsci.2013.09.003>.
- M. Atapour, A. Pilchak, G.S. Frankel, J.C. Williams, M.H. Fathi, M. Shamanian, Corrosion behavior of Ti-6Al-4V with different thermomechanical treatments and microstructures, *Corrosion* 66 (2010) 065004–065004-9, <https://doi.org/10.5006/1.3452400>.
- N. Dai, L.-C. Zhang, J. Zhang, Q. Chen, M. Wu, Corrosion behavior of selective laser melted Ti-6Al-4V alloy in NaCl solution, *Corros. Sci.* 102 (2016) 484–489, <https://doi.org/10.1016/j.corsci.2015.10.041>.
- R.M. Abou Shahba, W.M. Ghannem, A. El-Sayed El-Shenawy, Corrosion and inhibition of Ti-6Al-4V alloy in NaCl solution, *Int. J. Electrochem. Sci.* 6 (2011) 5499–5509.
- Z. Liu, M. Curioni, P. Jamshidi, A. Walker, P. Prengnell, G.E. Thompson, P. Skeldon, Electrochemical characteristics of a carbon fibre composite and the associated galvanic effects with aluminium alloys, *Appl. Surf. Sci.* 314 (2014) 233–240, <https://doi.org/10.1016/j.apsusc.2014.06.072>.
- R. Srinivasan, J.A. Nelson, L.H. Hihara, Development of guidelines to attenuate galvanic corrosion between mechanically-coupled aluminium and carbon-fiber reinforced epoxy composites using insulation layers, *J. Electrochem. Soc.* 162 (2015) C545–C554, <https://doi.org/10.1149/2.0611510jes>.
- R. Srinivasan, L.H. Hihara, Utilization of hydrophobic coatings on insulative skirts to attenuate galvanic corrosion between mechanically-fastened aluminium alloy and carbon-fiber reinforced polymer-matrix composites, *Electrochem. Commun.* 72 (2016) 96–99, <https://doi.org/10.1016/j.elecom.2016.09.014>.
- L.B. Coelho, M. Taryba, M. Alves, M.F. Montemor, M. Olivier, Unveiling the effect of the electrodes area on the corrosion mechanism of a graphite - AA2024-T3 galvanic couple by localised electrochemistry, *Electrochim. Acta* 277 (2018) 9–19, <https://doi.org/10.1016/j.electacta.2018.04.187>.
- L.B. Coelho, M.G. Olivier, The inhibition efficiency of different species on AA2024/graphite galvanic coupling models depicted by SVET, *Corros. Sci.* 136 (2018) 292–303, <https://doi.org/10.1016/j.corsci.2018.03.015>.
- F. Bellucci, A. Di Martino, C. Liberti, Electrochemical behaviour of graphite-epoxy composite materials (GECM) in aqueous salt solutions, *J. Appl. Electrochem.* 16 (1986) 15–22, <https://doi.org/10.1007/BF01015979>.
- F. Bellucci, Galvanic corrosion between nonmetallic composites and metals II. Effect of area ratio and environmental degradation, *Corrosion* 48 (1992) 281–291, <https://doi.org/10.5006/1.3315934>.
- S. Payan, Y. Le Petitcorps, J.-M. Olive, H. Saadaoui, Experimental procedure to analyse the corrosion mechanisms at the carbon/aluminium interface in composite materials, *Compos. Part A* 32 (2001) 585–589, [https://doi.org/10.1016/S1359-835X\(00\)00126-3](https://doi.org/10.1016/S1359-835X(00)00126-3).
- M. Serdechnova, S. Kallip, M.G.S. Ferreira, M.L. Zheludkevich, Active self-healing coating for galvanically coupled multi-material assemblies, *Electrochem. Commun.* 41 (2014) 51–54, <https://doi.org/10.1016/j.elecom.2014.01.023>.
- Y. Pan, G. Wu, X. Cheng, Z. Zhang, M. Li, S. Ji, Z. Huang, Galvanic corrosion behaviour of carbon fibre reinforced polymer/magnesium alloys coupling, *Corros. Sci.* 98 (2015) 672–677, <https://doi.org/10.1016/j.corsci.2015.06.024>.
- Z. Peng, X. Nie, Galvanic corrosion property of contacts between carbon fiber cloth materials and typical metal alloys in an aggressive environment, *Surf. Coatings Technol.* 215 (2013) 85–89, <https://doi.org/10.1016/j.surfcoat.2012.08.098>.
- F. Bellucci, Galvanic corrosion between nonmetallic composites and metals: I effect of metal and of temperature, *Corrosion* 47 (10) (1991) 808–819, <https://doi.org/10.5006/1.3585192>.
- B.A. Miller Jr, *The Galvanic Corrosion of GECM Coupled with Alloys*, (1975) Report number GAME/C/75D-8.
- Y.C. Webster RT, *Industrial Applications of Titanium and Zirconium: Third Conference*, ASTM International, 100 Barr Harbor Drive, PO Box C700, West Conshohocken, PA 19428-2959, 1984, <https://doi.org/10.1520/STP830-EB>.
- M. Atapour, A.L. Pilchak, M. Shamanian, M.H. Fathi, Corrosion behavior of Ti-8Al-1Mo-1V alloy compared to Ti-6Al-4V, *Mater. Des.* 32 (2011) 1692–1696, <https://doi.org/10.1016/j.matdes.2010.09.009>.
- V. Astanin, D. Nurullina, A. Zaripova, P. Soloviev, F. Musin, Carbon fiber reinforced magnesium alloy in a Ti-6Al-4V shell, *MATEC Web Conf.* 129 (2017) 02018, <https://doi.org/10.1051/mateconf/201712902018>.
- F. Mansfeld, E.P. Parry, Galvanic corrosion of bare and coated Al alloys coupled to stainless steel 304 or Ti-6Al-4V, *Corros. Sci.* 13 (1973) 605–621, [https://doi.org/10.1016/S0010-938X\(73\)80027-7](https://doi.org/10.1016/S0010-938X(73)80027-7).
- A. de Rooij, Bimetallic compatible couples, *ESA J.* 13 (1989) 199–209 <http://www.scopus.com/inward/record.url?eid=2-s2.0-0024917598&partnerID=40&md5=f2ce6bcb2eac5b3a373c83247ebada5>.
- G. Williams, A.J. Coleman, H.N. McMurray, Inhibition of aluminium alloy AA2024-T3 pitting corrosion by copper complexing compounds, *Electrochim. Acta.* 55 (2010) 5947–5958, <https://doi.org/10.1016/j.electacta.2010.05.049>.
- J. Yang, H. Yang, H. Yu, Z. Wang, X. Zeng, Corrosion behavior of additive manufactured Ti-6Al-4V alloy in NaCl solution, *Metall. Mater. Trans. A.* 48 (2017) 3583–3593, <https://doi.org/10.1007/s11661-017-4087-9>.
- M. Textor, C. Sittig, V. Frauchiger, S. Tosatti, D.M. Brunette, Properties and Biological Significance of Natural Oxide Films on Titanium and Its Alloys, (2001), pp. 171–230, https://doi.org/10.1007/978-3-642-56486-4_7.
- A. Boag, R.J. Taylor, T.H. Muster, N. Goodman, D. McCulloch, C. Ryan, B. Rout, D. Jamieson, A.E. Hughes, Stable pit formation on AA2024-T3 in a NaCl environment, *Corros. Sci.* 52 (2010) 90–103, <https://doi.org/10.1016/j.corsci.2009.08.043>.
- A. Boag, A.E. Hughes, A.M. Glenn, T.H. Muster, D. McCulloch, Corrosion of AA2024-T3 part I: localised corrosion of isolated IM particles, *Corros. Sci.* 53 (2011) 17–26, <https://doi.org/10.1016/j.corsci.2010.09.009>.
- J. Li, N. Birbilis, R.G. Buchheit, Electrochemical assessment of interfacial characteristics of intermetallic phases present in aluminium alloy 2024-T3, *Corros. Sci.* 101 (2015) 155–164, <https://doi.org/10.1016/j.corsci.2015.09.012>.
- A.G. Marques, M.G. Taryba, A.S. Panão, S.V. Lamaka, A.M. Simões, Application of scanning electrode techniques for the evaluation of iron-zinc corrosion in nearly neutral chloride solutions, *Corros. Sci.* 104 (2016) 123–131, <https://doi.org/10.1016/j.corsci.2015.12.002>.
- A.L. Correa-Borroel, S. Gutierrez, E. Arce, R. Cabrera-Sierra, P. Herrasti, Organosilanes and polypyrrole as anticorrosive treatment of aluminium 2024, *J. Appl. Electrochem.* 39 (2009) 2385–2395, <https://doi.org/10.1007/s10800-009-9925-z>.
- M. Machkova, E.A. Matter, S. Kozhukharov, V. Kozhukharov, Effect of the anionic part of various Ce(III) salts on the corrosion inhibition efficiency of AA2024 aluminium alloy, *Corros. Sci.* 69 (2013) 396–405, <https://doi.org/10.1016/j.corsci.2013.01.008>.
- M.A. Amin, Metastable and stable pitting events on Al induced by chlorate and perchlorate anions-polarization, XPS and SEM studies, *Electrochim. Acta.* 54 (2009) 1857–1863, <https://doi.org/10.1016/j.electacta.2008.10.009>.
- J. Li, B. Hurlley, R. Buchheit, Effect of temperature on the localized corrosion of AA2024-T3 and the electrochemistry of intermetallic compounds during exposure to a dilute NaCl solution, *Corrosion* 72 (2016) 1281–1291, <https://doi.org/10.5006/2136>.
- T. Suter, R.C. Alkire, Microelectrochemical studies of pit initiation at single inclusions in Al 2024-T3, *J. Electrochem. Soc.* 148 (2001) B36, <https://doi.org/10.1149/1.1344530>.
- M. Schneider, K. Kremmer, C. Lämmel, K. Sempf, M. Herrmann, Galvanic corrosion of metal/ceramic coupling, *Corros. Sci.* 80 (2014) 191–196, <https://doi.org/10.1016/j.corsci.2013.11.024>.
- M. Metikoš-Huković, I. Milošev, Electrochemical methods in the study of localized corrosion attack, *J. Appl. Electrochem.* 22 (1992) 448–455, <https://doi.org/10.1007/BF01077548>.